Arabian Journal of Chemistry (2020) 13, 7357–7369

King Saud University

Arabian Journal of Chemistry

www.ksu.edu.sa
www.sciencedirect.com

ORIGINAL ARTICLE

Study of oxidative dehydrogenation of ethylbenzene with CO_2 on supported CeO_2-Fe_2O_3 binary oxides

Kechen Song [a], **Shuo Wang** [b], **Qiang Sun** [b], **Deping Xu** [a,*]

[a] *School of Chemical and Environmental Engineering, China University of Mining and Technology (Beijing), Beijing 100083, China*
[b] *Department of Materials Science and Engineering, College of Engineering, Peking University, Beijing 100871, China*

Received 18 June 2020; revised 11 August 2020; accepted 12 August 2020
Available online 25 August 2020

KEYWORDS

CeO_2-Fe_2O_3 binary oxides;
Solid solution;
Ethylbenzene dehydrogenation;
Oxygen mobility;
DFT

Abstract Nano-sheets Al_2O_3 supported CeO_2-Fe_2O_3 binary oxides were prepared by the vacuum impregnation method. The structural and textural properties were characterized by pertinent techniques, and the materials were evaluated as catalysts for the oxidative dehydrogenation of ethylbenzene with carbon dioxide (CO_2-ODEB). The characterization results show that all samples maintain the hierarchical structure, and CeO_2-like and Fe_2O_3-like solid solutions were formed when changing the Ce-to-Fe molar ratio. The catalytic performances indicate that CeO_2-Fe_2O_3 binary oxides were effective for CO_2-ODEB, and the activity is determined by mobile oxygen, which can facilitate the dehydrogenation process. The DFT studies further identified the reaction pathway and rate-determining step. The inter-transmission of oxygen species and the presence of CO_2 refill the oxygen vacancies and restore the redox cycle of CeO_2-Fe_2O_3 binary oxides.

1. Introduction

Styrene, a very important raw material in the petrochemical industry, is used in the production of polymers, such as polystyrene and styrene-butadiene rubber, amongst many others (Lee, 1974; Baghalha and Ebrahimpour, 2007). Typically, styrene is produced by dehydrogenation of ethylbenzene, which requires an exorbitant supply of super-heated steam (Coulter et al., 1995; Wu et al., 1993). This process consumes a significant amount of energy and results in a challenging gas–liquid phase separation; the equilibrium efficiency is also quite low, with 79.7% ethylbenzene conversion occurring at the high temperature of 983 K. Due to these drawbacks, the replacement of steam with CO_2 is believed to be energy-saving and theoretically favorable (Zhao et al., 2007; Kuśtrowski et al., 2006). It has been reported that the utilization of CO_2 can reduce the required energy input from 6.27×10^6 to 7.9×10^5 kJ·ton^{-1}. Additionally, an estimation of energy required for steam-assisted and oxidative dehydrogenation of ethylbenzene suggests that the energy required in case of CO_2 utilization was very less (190 kcal/kg of styrene) compared to that of steam (1500 kcal/kg of styrene) (Mimura et al., 1998); second, the CO_2 utilization offers several advantages, such as enhancement of the product selectivity, diminishing of the thermodynamic limitations, suppression of the over oxidation. Furthermore, the coupling of oxidative dehydrogenation of ethylbenzene

* Corresponding author.
E-mail address: kcsong@umd.edu (D. Xu).
Peer review under responsibility of King Saud University.

ELSEVIER Production and hosting by Elsevier

https://doi.org/10.1016/j.arabjc.2020.08.013
1878-5352

with reverse water–gas shift reaction will improve the per-pass ethylbenzene conversion (Sun et al., 2004). In addition, the employment of CO_2 is environmentally friendly and could establish a greenhouse gas conversion approach (Ansari and Park, 2012).

Various catalysts have been investigated for the CO_2-ODEB (Brünig et al., 2018; Diao et al., 2017, 2016; Liu et al., 2014). Among different type of catalysts, CeO_2-based materials have been extensively designed and used as catalyst due to the remarkable oxygen storage capacity (OSC) and enhanced redox properties (Wang et al., 2019a, 2019b; Fan et al., 2019; Kuntaiah et al., 2013; Kurnatowska et al., 2014; Zhou and Zhou, 2010). It has been shown that the substitution of Ce^{4+} by isovalent ions, like Zr^{4+} and Hf^{4+}, shows superior activity, so Ce-Zr solid solution is the most widely investigated catalyst in CO_2-ODEB (Su et al., 2018; Wang et al., 2017a). It is reported that introducing Zr^{4+} could lead to better lattice oxygen mobility and facile reduction of Ce^{4+}, moreover, the reducible tetravalent ions like Sn^{4+} and Ti^{4+} exhibit better activity than a non-reducible Zr-substitution (Yao et al., 2013). However, isovalent ions dopants can increase the difficulty in creating oxygen vacancies (Ahn et al., 2012). Therefore, there is considerable scientific interest in introducing aliovalent cations into CeO_2, such as Gd^{3+} and Sm^{3+}, as they can generate extrinsic oxygen vacancies via charge compensation mechanism (Guo et al., 2011). One possibility is to introduce trivalent ions with similar radius, such as Eu^{3+}, as a method of altering the characteristics. Another way is incorporating ions with an undersized radius, like Fe^{3+}, and the resulting material was also studied in numerous reactions (Kano et al., 2013; Li et al., 2001; Pérez-Alonso et al., 2005; Wang et al., 2014). As a well-suited reducible dopant, Fe has attracted attention because of its unique advantages, easy handling, and low-cost features (Hedayati et al., 2012; Hong et al., 2010; Liang et al., 2009; Zuo et al., 2013). In particular, the redox potential of Fe^{3+} and Fe^{2+} is 0.77 V, very much lower than that of Ce^{4+} and Ce^{3+}, 1.44 eV. (Hedayati et al., 2012). Zhang et al. proposed that the lattice oxygen in Fe_2O_3 participates in the reaction and reduces Fe^{3+} to Fe^{2+}, which is then restored by CeO_2 (Zhang et al., 2010). Singh reported the oxygen species in CeO_2-Fe_2O_3 binary oxides were more labile and Fe dopants into ceria lead to strong structural distortion and lower oxygen vacancy formation energy, thus to the resulting catalyst is suited for CO_2-ODEB (Kurnatowska et al., 2014).

There are two reported mechanisms for CO_2-ODEB. One is a coupling mechanism, which involves the direct dehydrogenation of ethylbenzene, followed by the reverse water–gas shift reaction. The other is Mars-van-Krevelen redox mechanism involving the lattice oxygen (Liu et al., 2011; Mimura and Saito, 2000). Previous studies suggested CeO_2-Fe_2O_3 binary oxides align best with the redox mechanism, where ethylbenzene reacts with mobile oxygen to produce styrene and water, simultaneously, a stoichiometric amount of oxygen vacancies is left over the oxide catalyst, which is then replenished by CO_2 to complete the redox cycle. Thus, the amount and reversibility of mobile oxygen are crucial in determining the activity.

In this work, an Al_2O_3 assembled by nanosheets, which presents the hierarchical structure and reported to be beneficial to the dispersion and both chemical and thermal stability (Wang et al., 2017a, 2017b), was used as support to prepare the supported CeO_2-Fe_2O_3 binary oxides, and evaluated as catalyst for the possible use in CO_2-ODEB. The reaction results reflected that the activity of the catalysts was correlated with their structural and redox properties. The physicochemical properties were then investigated and discussed to reveal the determining factors in the reaction.

2. Experimental

2.1. Material

Aluminum nitrate nonahydrate ($Al(NO_3)_3{\cdot}9H_2O$), cerium nitrate hexahydrate ($Ce(NO_3)_3{\cdot}6H_2O$), and iron nitrate nonahydrate ($Fe(NO_3)_3{\cdot}9H_2O$) were purchased from Alfa Aesar (USA), urea (CH_4N_2O) was purchased from Aladdin (Shanghai, China). Catalytic reaction solution of benzene, toluene, styrene, and were purchased from Sigma-Aldrich (USA). All the reagents are analytical grade and used directly without further purification.

2.2. Catalyst preparation

Nano-sheets of γ-Al_2O_3 were synthesized via a controlled hydrothermal method according to literature (Abdollahifar et al., 2014), and labeled as NSA. The synthetic steps are as follows, 18.75 g of $Al(NO_3)_3{\cdot}9H_2O$ and 6 g of urea, CH_4N_2O, were dissolved in 100 and 30 mL of distilled water, respectively, and magnetically stirred at room temperature to obtain homogeneous solutions A and B. Then solution B was added to solution A and stirred at room temperature for 15 min, then transferred the mixed solution into a 200 mL Teflon-lined stainless autoclave and heated at 473 K for 24 h under autogenous pressure. After being naturally cool down to room temperature, the precipitate was filtered, washed three times with distilled water, and finally dried in an oven at 333 K for 24 h, then calcined at 773 K in air for 5 h.

A series of CeO_2-Fe_2O_3 binary oxides with different molar ratios were loaded onto the supports. The synthesis of Ce50Fe50/NSA was explained as an example of the detailed synthesis. 0.43 g $Ce(NO_3)_3{\cdot}6H_2O$ and 0.42 g $Fe(NO_3)_3{\cdot}9H_2O$ were dissolved in 10 mL deionized water, respectively (Ce/Fe molar ratio = 1.0, Ce + Fe = 0.002 mol), then mixed above solutions and magnetic stirred for 30 min, then 5.0 g nanosheets Al_2O_3 were dispersed into the solution under stirring, after 30 min ultrasonic processing, the resulting mixture was moved to a vacuum rotary evaporator, set to 343 K and 50 round per minute for 10 h. Finally, the obtained solids were calcined at 873 K in static air for 5 h at the heating rate of 1 $K{\cdot}min^{-1}$, leading to the 5 wt% Ce50Fe50/NSA. By simply changing the amount of $Ce(NO_3)_3{\cdot}6H_2O$ and $Fe(NO_3)_3{\cdot}9H_2O$, the CexFe(100-x)/NSA (x = 0, 10, 30, 50, 70, 100) was synthesized, using the same procedure and parameters.

2.3. Characterization

Field emission scanning electron microscopy (FESEM) images were obtained on a Zeiss Supra 55 microscope. Transmission electrons were recorded on a FEI Tecnai G2-20 S-TWIN. The surface areas of the materials were determined by the BET method using an automatic Micromeritics ASAP 2020M. Before measurement, the samples were degassed at

473 K for 8 h, and the N_2 adsorption–desorption was performed at 77 K. X-ray diffraction (XRD) patterns were recorded on a Rigaku X-ray diffractometer (D/Max 2550VB +/PC) equipped with Cu/Kα radiation Cu/Kα (40 kV, 30 mA). The samples were scanned from 2θ of 10-90° with a step size of 0.02○ and a counting time of 2.5 s per step. The X-ray photoelectron spectroscopy (XPS) analysis was performed on a KRATOS Axis Ultra DLD spectrometer with an Mg Kα radiation from a double anode X-ray source. The binding energy correction was made using the adventitious C 1s at 284.5 eV as a reference for all the elements recorded. The reduction behavior of the composite oxides was investigated by hydrogen temperature-programmed reduction (TPR) in a Micromeritics Autochem 2920 instrument. Firstly, 50 mg of each sample was loaded and flushed with an Ar flow of 30 mL·min^{-1} at room temperature for 2 h and then increased from room temperature to 1273 K at a temperature ramp rate of 10 K·min^{-1} under 30 mL·min^{-1} flow of 10 vol% H_2 in Ar. After condensing the water formed in a liquid N_2 trap, the effluent was monitored with a TCD detector. The spent catalysts were characterized by the thermogravimetric analysis technique on a Netzsch STA 449 F5 thermo analyzer system (TA Instruments). The sample (ca. 10 mg) was heated at a rate of 10 K·min^{-1} under a constant flow of CO_2 (50 mL·min^{-1})

2.4. Simulation details

The first-principles calculations have been performed by the VASP code (Kresse and Furthmüller, 1996; Kresse and Hafner, 1993). The generalized gradient approximation functional proposed by Perdew et al. was used (Perdew et al., 1996). The interactions between valence electrons and ion cores are represented by Blöchl's all-electron-like projector augmented wave method (PAW), which regards the d7s1 states as the valence configuration for Fe, s2p4 for O, 4f15d16s2 for Ce and s2p2 for C (Blöchl, 1994). A plane wave energy cutoff of 400 eV was used in the present calculations. Geometries were relaxed using the conjugate gradient algorithm until the forces on all the unconstrained atoms are less than 0.03 eV/Å (Sheppard et al., 2008).

2.5. Catalytic reaction procedure

The oxidative dehydrogenation of ethylbenzene with CO_2 was performed in a quartz fixed-bed reactor with an internal diameter of 6 mm, housed inside an electric furnace with three independently controlled temperatures zones. The temperature of the catalyst bed was measured by K-type thermocouple. A fritted quartz disk placed in the center of the reactor was used to hold the catalyst. Typically, 0.3 g catalyst (40–60 mesh) diluted with the same amount of quartz sands was loaded into the reactor, then heating up under N_2 flow, when reached the reaction temperature, the catalyst was pre-treated at the reaction temperature for 30 min under flowing CO_2 to remove the physically absorbed impurities and N_2. The analytical grade ethylbenzene (99.999% purity) was then introduced into a gasifier using a HPLC pump at a flow rate of 0.006 mL·min^{-1}, then the vaporized ethylbenzene carried by CO_2 flow was fed into the reactor. The reaction temperature was 823 K, P = 0.1 MPa, total flow rate = 25 mL·min^{-1}, CO_2/EB molar ratio = 20, W/F = 4.747 g-cat·h·mol^{-1}. The condensed products, including benzene (BE), toluene (TO), styrene (ST), and unreacted ethylbenzene (EB), were analyzed on a gas chromatograph equipped with a DB-1 capillary column (0.25 mm × 60 m) and an FID detector. The ethylbenzene conversion and styrene selectivity were calculated based on the calibrated GC peak areas of the components. The following expressions were used to determine the activity of different catalysts. The percent conversion for a reactant (Eq. (1)) and selectivity towards a product (Eq. (2)) were calculated as:

$$\text{Ethylbenzene conversion} = \frac{C_{EB,inlet} - C_{EB,outlet}}{C_{EB,inlet}} \quad (1)$$

$$\text{Styrene selectivity} = \frac{C_{ST,outlet}}{C_{EB,inlet} - C_{EB,outlet}} \quad (2)$$

$C_{EB,\ inlet}$ is the ethylbenzene concentration in the feed before the reaction and $C_{EB,\ outlet}$ is the ethylbenzene concentration in the product; $C_{ST,\ outlet}$ is the styrene concentration in the product.

3. Results and discussion

3.1. Structure of supported CeO_2-Fe_2O_3 binary oxides

To investigate the textural properties of the supported CeO_2-Fe_2O_3 binary oxides, N_2 adsorption–desorption isotherms were measured and shown in Fig. 1(A). All the isotherms exhibited IV type behavior with an H3 hysteresis loop, indicating the presence of slit-shaped pores associated with the unique structure of the support. Clearly, after the loading of CeO_2-Fe_2O_3 binary oxides, the adsorption volume decreased when compared to the unloaded support, indicating that the CeO_2-Fe_2O_3 binary oxides were located in the slit pores of the nanosheets support. Additionally, in the low relative pressure range, the uptake of supported samples was lower than pristine support, which suggested the occupation of the micropores.

The pore size distributions (PSD) plot, as shown in Fig. 1 (B), further underscored the textural properties. The pore size distribution curves were determined from the adsorption branch of N_2 isotherms. All the samples showed a similar peak center at 3–5 nm, together with the presence of broad distribution consisting of wide mesopores and macropores, which means the hierarchical porous structure; no significant variation means the hierarchical structure was maintained after CeO_2-Fe_2O_3 binary oxides loading.

The physical textural parameters were collected in Table 1. It was interesting to see that sample Ce0Fe100/NSA lost a lot of pore volume but kept a relatively high surface area, potentially due to agglomerated FeO_x blocked the larger-sized mesopores which contribute little to the external surface area, while the smaller-sized mesopores were left intact (Oh et al., 2017), this is also supported by the PSD curve. For other samples, with the increase of Ce content, both surface area and pore volume decreased, which indicates that CeO_2-Fe_2O_3 binary oxides were not only located on the outermost surface but also entered the slit-shaped pores. These changes may be ascribed to the unique porosity derived from the nano-sheets-like architecture, since the material can retain the accessibility to the

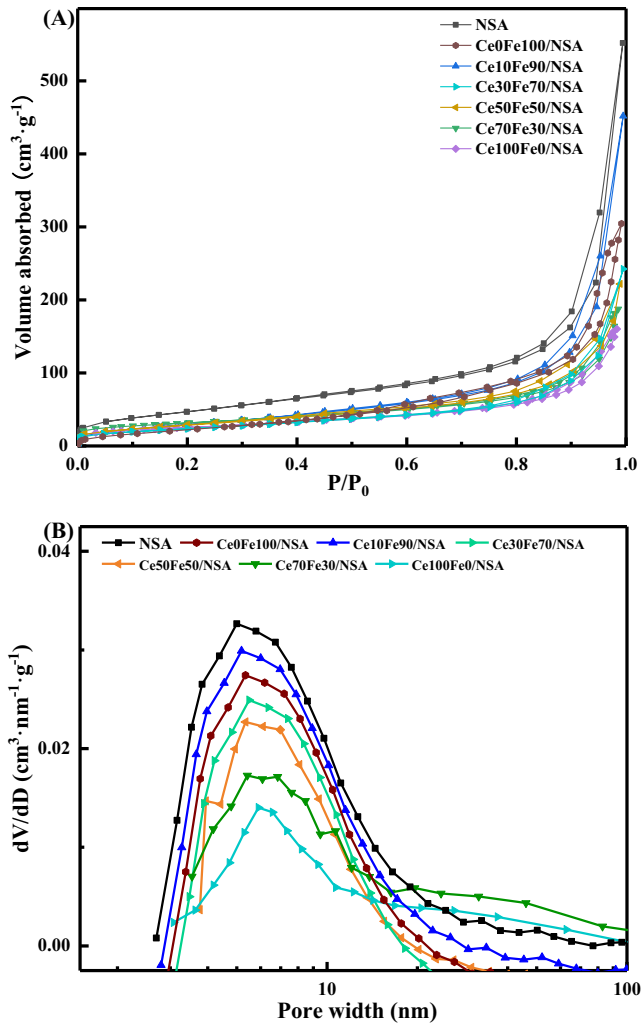

Fig. 1 (A) N_2 adsorption–desorption isotherms and (B) pore size distributions of NSA and supported CeO_2-Fe_2O_3 binary oxides.

internal pores and decrease the possibility of blocking, therefore providing the potential for high dispersion (Wang et al., 2017b).

Table 1 Textural properties of NSA and supported CeO_2-Fe_2O_3 binary oxides.

Catalyst	V_{total} [$cm^3 \cdot g^{-1}$]	S_{BET} [$m^2 \cdot g^{-1}$]	Mean pore diameter [nm]
NSA	0.85 ± 0.04	177.43 ± 8.87	4.32 ± 0.22
Ce0Fe100/NSA	0.42 ± 0.02	130.41 ± 6.62	3.81 ± 0.19
Ce10Fe90/NSA	0.51 ± 0.02	119.90 ± 5.99	3.64 ± 0.18
Ce30Fe70/NSA	0.38 ± 0.01	100.24 ± 5.01	3.62 ± 0.18
Ce50Fe50/NSA	0.35 ± 0.01	94.89 ± 4.74	3.38 ± 0.17
Ce70Fe30/NSA	0.33 ± 0.01	107.7 ± 5 0.38	3.41 ± 0.16
Ce100Fe0/NSA	0.27 ± 0.01	87.7 ± 4.38	3.43 ± 0.17

3.2. Crystal properties

Supported CeO_2-Fe_2O_3 binary oxides and pure Fe_2O_3/CeO_2 loaded crystalline structure after calcination at 873 K was investigated by XRD, and the spectra are presented in Fig. 2. The reflections can be assigned either to hematite, α-Fe_2O_3 (hexagonal, JCPD 33-0664), or cubic CeO_2 (fluorite, JCPDS 65-5923) (Yin et al., 2012). In Ce0Fe100/NSA, typical patterns of hexagonal hematite structure were observed, however, peaks derived from NSA support were weak and occurred as a bump, this may shed some light on textural properties discussed above. For Ce10Fe90/NSA, the diffraction peaks assigned to Fe_2O_3 showed higher intensity than those in Ce0Fe100/NSA, and peaks of support occurred, meanwhile, the cubic CeO_2 peaks were missing. With increasing of Ce-to-Fe molar ratio, the CeO_2 peaks were identified and became stronger, in addition, sample Ce50Fe50/NSA still showed weak Fe_2O_3 peaks, while Ce70Fe10/NSA barely exhibited α-Fe_2O_3 peaks, with only CeO_2 peaks appearing in the spectrum. It should be noted that the characteristic peak of CeO_2 shifted towards lower 2θ position in some samples with the increase of Ce-to-Fe molar ratio, as shown in the left enlarged portion of Fig. 2, which, combined with absent Fe_2O_3 peaks, that may suggest the formation of solid solution or highly dispersed Fe_2O_3 (Zhu et al., 2014, 2013).

To further verify the formation of the solid solution, the unit cell parameters of each sample were calculated using Scherrer's equation (Patterson, 1939) and collected in Table 2. The spectra from some samples were not suitable to accurately determine the unit cell parameters due to the low peak intensities. From Table 2, a shrinkage in CeO_2 lattice constants was observed, indicating a CeO_2-like solid solution was initially formed in Ce30Fe70/NSA, Ce50Fe50/NSA, and Ce70Fe30/NSA, as some Ce^{4+} in the CeO_2 lattice were substituted by Fe^{3+}, since the Fe^{3+} cation size is smaller than Ce^{4+} (0.0645 and 0.102 Å). On the other hand, increased peak intensity also reflected the increased concentration of CeO_2-like solid solution (Pérez-Alonso et al., 2006). As for the hematite, the lattice constants also exhibited an increasing trend with the rising of the Ce-to-Fe molar ratio. This phenomenon can be explained by the incorporation of Ce cations into the hematite lattice, leading to the expansion, especially for the parameter *c*. Besides, this change can be verified by the shift of hematite characteristic peaks, as shown in the enlarged middle portion.

3.3. Morphologic characteristics

TEM and FESEM were performed to explore the morphology of NSA support and loaded samples. It is important to note that the calculation of the particle size from TEM images was rather difficult as there were no protective agents used, so no precise calculations were attempted in this study.

As shown in Fig. 3(a) and (b), the NSA supports consist of a great deal of nano-sheets-like architecture with an average size of about 476 × 226 × 42 nm (length × width × thickness). Fig. 3(c) and (d) were supported CeO_2-Fe_2O_3 binary oxides, Ce10Fe90/NSA and Ce70Fe30/NSA, which appeared as a homogeneous agglomeration of particles. Sample Ce10Fe90/NSA showed a number of small particles (~5–7 nm) with a clear grain boundary supported on a larger particle (> 20 nm), whose lattice fringe with an interplanar spacing

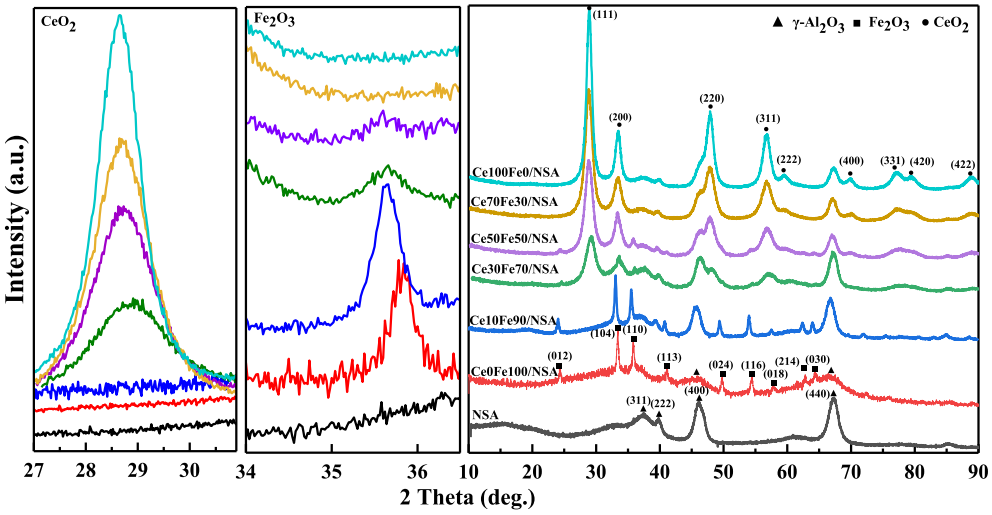

Fig. 2 XRD patterns of NSA and supported CeO_2-Fe_2O_3 binary oxides.

Table 2 Unit cell parameters of supported CeO_2-Fe_2O_3 binary oxides.

Sample	Crystallite size (nm)	Lattice constant (nm)	
		CeO_2	Fe_2O_3
Ce0Fe100/NSA	15.57	–	*a* 0.6404 *c* 1.4059
Ce10Fe90/NSA	8.30	–	*a* 0.6563 *c* 1.4127
Ce30Fe70/NSA	8.60	*a* 0.5414	*a* 0.6780 *c* 1.4245
Ce50Fe50/NSA	8.84	*a* 0.5436	*a* 0.6815 *c* 1.4625
Ce70Fe30/NSA	9.35	*a* 0.5457	– –
Ce100Fe0/NSA	9.40	*a* 0.5519	–

of ~0.27 nm was associated with the (1 1 0) facet of Fe_2O_3. The Ce70Fe30/NSA sample displayed a notably different morphology from that of Ce10Fe90/NSA, and showed a lattice fringe of ~0.31 nm, which can be attributed to the cubic CeO_2 (1 1 1) at 28.6° crystal planes.

3.4. Reduction behavior

As a matter of fact, the OSC and its mobility were closely related to the reducibility and defects. To gain further insight into the composition and structure, supported CeO_2-Fe_2O_3 binary oxides were investigated via H_2-TPR, and the results were shown in Fig. 4. The hydrogen reduction of Fe_2O_3 is commonly reported to be stepwise, where Fe^{3+} converts to metallic Fe by going through Fe_3O_4 and FeO as intermediates. In the current study, peaks of the pure Fe_2O_3 loaded sample correspond to the above process at about 673, 923, and 1123 K. For pure CeO_2, mainly two reduction steps, the reduction of surface-capping oxygen at about 793 K and the reduction of bulk phase oxygen reduction at about 1173 K, where, in the presently studied sample, Ce100Fe0/NSA only displayed the high-temperature reduction peak, surface oxygen barely existed.

For CeO_2- Fe_2O_3 binary oxides, according to Lagun and Qiao (Laguna et al., 2011; Qiao et al., 2011), four well-defined reduction peaks at around 673, 873 and 1073 K corresponded to the Fe^{3+} and Ce^{4+} reduction in solid solution, Fe species intermediate reduction step, and bulk Ce^{4+} reduction, respectively. As shown in Fig. 4, sample Ce70Fe30/NSA, the XRD pattern was essentially the same as that of pure CeO_2 loaded sample, but the reducibility was improved, as observed the significantly lowered first reduction temperature, likely due to the doping of Fe^{3+} into the CeO_2 lattice and the strong metal-support interaction enhancing the reducibility (Ebiad et al., 2012; Figueiredo et al., 2019). For the sample Ce50Fe50/NSA, Ce30Fe70/NSA, and Ce10Fe90/NSA, the first peak could result from the reduction of segregated FeO_x, and peak area was proportional to the Fe content. The shoulder peak appeared in Ce50Fe50/NSA and Ce10Fe90/NSA was due to the reduction of surface CeO_2, which closely contacted with the surface segregated FeO_x, and the peak area was increased with Ce-to-Fe molar ratio. The broad peak in the range of 723 to 973 K was ascribed to the Fe species intermediate reduction step, and the last peak at higher temperature was due to the reaction of bulk CeO_2.

3.5. Surface composition

The XPS measurements were conducted to investigate the surface composition, and the results were plotted in Fig. 5. Fig. 5 (A) depicted the Ce 3d spectrum, and it is known to be complex in CeO_2-Fe_2O_3 binary oxides due to the hybridization of Ce 4f with ligand orbitals and fractional occupancy of the valence 4f orbitals, which assists the multiplet splitting of peaks into doublets showing further spectral activity due to final state effects. There were 8 peaks related to four different spin–orbit-split doublets. Among them, peaks denoted as U, U'' and U''' were attributed to Ce^{4+} $3d_{3/2}$, located at about 901.3, 907.3 and 916.9 ± 0.1 eV, and those denoted as V, V'' and V''' arisen from Ce^{4+} $3d_{5/2}$, located at about 882.7,

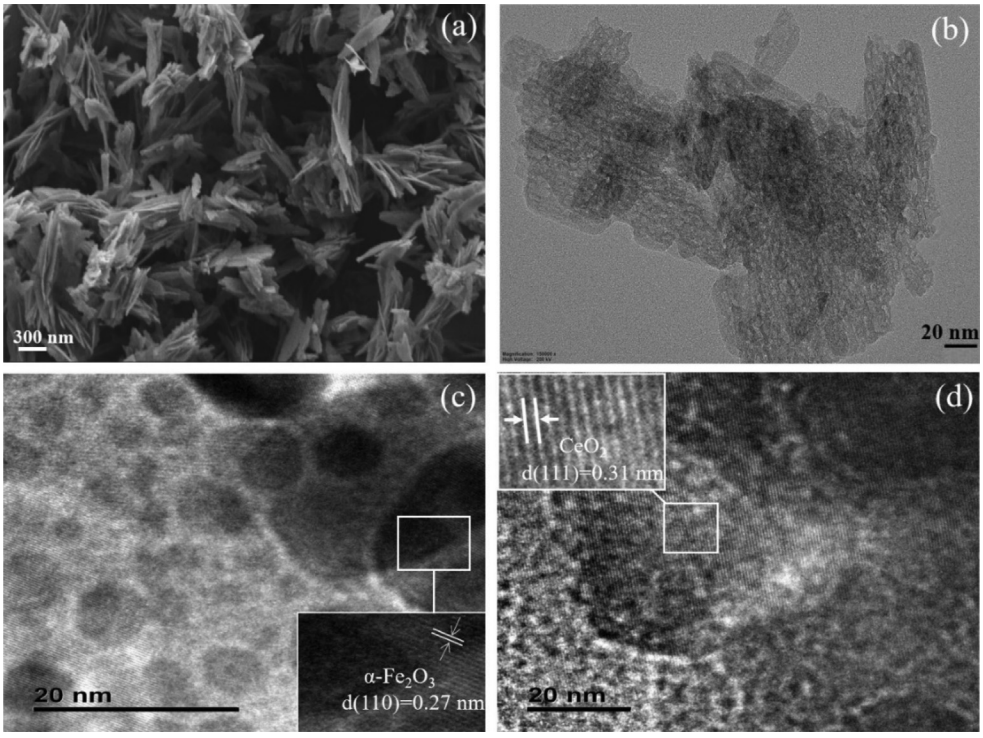

Fig. 3 SEM image of (a) NSA, TEM images of (b) NSA, (c) Ce10Fe90/NSA, and (d) Ce70Fe30/NSA.

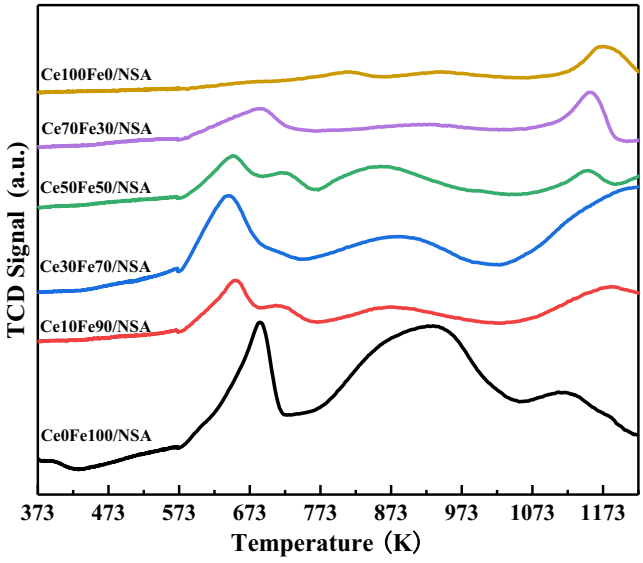

Fig. 4 H_2-TPR profiles of supported CeO_2-Fe_2O_3 binary oxides.

888.5 and 898.3 ± 0.1 eV, The pair of doublets, U' and V', were characterized by the lower binding energy intensities of Ce^{3+} $3d_{3/2}$ and Ce^{3+} $3d_{5/2}$, located at about 903.4 and 885.2 ± 0.1 eV (Bêche et al., 2008). As shown, CeO_2-Fe_2O_3 binary oxides containing both Ce^{4+} and Ce^{3+}, suggesting the rapid oxygen exchange and contributes to the enhancement of OSC. The Fe 2p spectrum, as shown in Fig. 5(B), two bands can be observed, which correspond to lower energy (Fe 2p3/2) and higher energy (Fe 2p1/2) asymmetric bands originated from the spin-orbital splitting. According to the literature, the standard Fe 2p3/2/Fe 2p1/2 signals corresponding to metallic iron, ferrous and ferric states are located at 706.7/719.8, 709.2/722.8 and 711.2/724.8 eV, respectively. Satellites peaks at 718 and 733 eV were also detected.

The binding energy and concentration of each element on the surface of samples were calculated based on the peak area and shown in Table 3. The binding energy of Al 2p increased slightly compared with the pristine support, possibly due to the effects of different Fe/Ce molar ratios on the final material properties, which could account for the appearance of unsaturated Al species derived from the removal of hydroxyl groups on the surface of NSA (Wang et al., 2017b). Taking the loading of Fe and Ce species into consideration, the interaction between binary oxides and support could also contribute to these changes. Moreover, the Fe/Al and Ce/Fe value varied with different Ce-to-Fe molar ratios, which reflects the dispersion variations and different O species content. The (Ce + Fe)/Al ratio remained constant due to the sum of Ce and Fe were constant. On the other hand, the content of Ce^{3+} on the surface of CeO_2-Fe_2O_3 binary oxides was strongly dependent on the Ce/Fe ratio. To make a quantitative comparison, the relative content of Ce^{3+} defined as the ratio of $Ce^{3+}/(Ce^{3+}+Ce^{4+})$ was calculated based on the peak area. By doping a small amount of Fe into CeO_2, the content of Ce^{3+} was increased from 20.04 to 27.17. The oxygen vacancy is believed result from the reduction of Ce^{4+} to Ce^{3+}, which will generate one oxygen vacancy to balance the charge, and thus the $Ce^{3+}/(Ce^{3+}+Ce^{4+})$ ratio could depict the concentration (Guo et al., 2011).

3.6. Catalytic performance

The catalytic performance of supported CeO_2-Fe_2O_3 binary oxides and pure CeO_2/Fe_2O_3 loaded samples were shown in

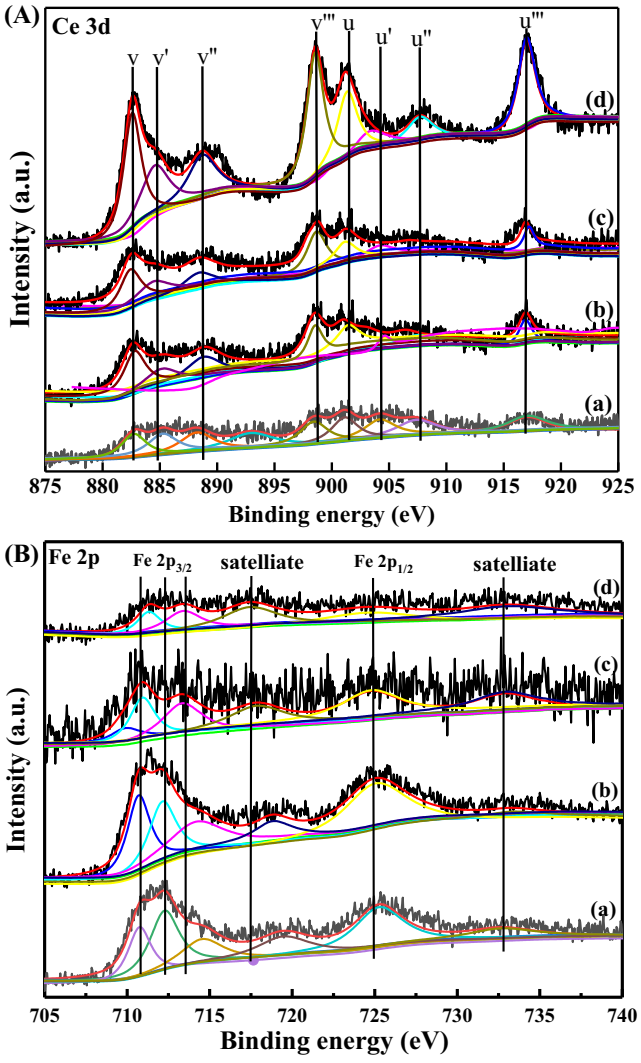

Fig. 5 Ce 3d (A) and Fe 2p (B) XPS spectra of (a) Ce10Fe90/NSA, (b) Ce30Fe70/NSA, (c) Ce50Fe50/NSA and (d) Ce70Fe30/NSA.

Fig. 6. All samples displayed a high steady-state selectivity of styrene above 90% under the optimized reaction condition. When the initial activity was considered, except pure CeO_2 loaded sample, all other samples showed around 55% ethylbenzene conversion. Ce30Fe70/NSA and Ce50Fe50/NSA displayed relatively higher and stable ethylbenzene conversion, while that of Ce70Fe30/NSA displayed a lower activity and

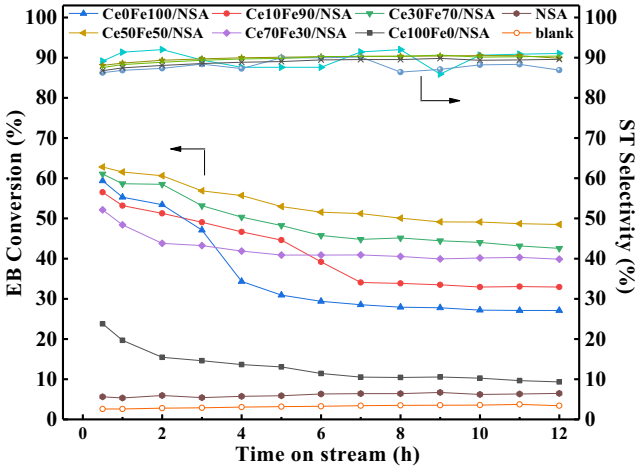

Fig. 6 Catalytic performance of supported CeO_2-Fe_2O_3 binary oxides for CO_2-ODEB. (823 K, P = 0.1 MPa, CO_2/EB molar ratio = 20, EB = 0.006 mL·min^{-1}).

stabilized gradually with TOS. For the sample Ce10Fe90/NSA and Ce0Fe100/NSA, suffer from the deactivation drastically, the EB conversion dropped more than 50% after 8 h TOS. Several related reported catalysts were listed in Table 4. Activity comparison of these cited catalysts such as Al_2O_3 supported Ce-Zr mixed oxides synthesized with impregnation and hydrothermal methods (Wang et al., 2019b, 2017b), vanadium-ceria-zirconia-alumina (Wang et al., 2019c), pure α-Fe_2O_3 (Wang et al., 2017c) and MnO_x (Ren et al., 2017), respectively, indicate that the present studied nanosheets Al_2O_3 supported CeO_2-Fe_2O_3 binary oxides show both higher activity and stability, could be a desired catalyst for CO_2-ODEB.

Additionally, the effect of feed gas was also studied. The catalytic test of sample Ce50Fe50/NSA was performed under N_2 flow, and the results were displayed in Fig. 7. The results indicated that CO_2 has a significant influence, as the styrene selectivity only dropped slightly, while the EB conversion under title reaction condition was much lower than under CO_2 flow. The detailed discussion was made correlated to the reaction mechanism in the later section.

Taking the redox mechanism into consideration, higher activity was expected due to the mobile oxygen species (Zhang et al., 2010). And normally, the general mobile oxygen should be primarily related to both lattice and

Table 3 Surface composition of supported CeO_2-Fe_2O_3 binary oxides.

Sample	Surface atomic ratio (%)				
	Al 2p	Fe/Al	Ce/Fe	(Ce + Fe)/Al	$Ce^{3+}/(Ce^{3+} + Ce^{4+})$
NSA	71.8	–	–	–	–
Ce10Fe90/NSA	74.1	0.029	0.10	0.12	20.04
Ce30Fe70/NSA	74.2	0.021	0.32	0.11	23.04
Ce50Fe50/NSA	74.3	0.018	0.92	0.13	26.04
Ce70Fe30/NSA	74.2	0.012	2.20	0.11	27.17

Table 4 Comparison studies of catalytic activity with reported catalysts.

Catalyst	Reaction Conditions		EB Con. (%)	ST Sel. (%)	Ref.
	Temperature (K)	Atmosphere			
Ce-Zr/NFA	823	CO_2	53	95	Wang et al. (2017a)
Fe/FA	823	CO_2	38	> 95	Wang et al. (2017b)
$Ce_{1-x}Fe_xO_2$	823	CO_2	35	92	Wang et al. (2014)
$Ce_{1-x}Zr_xO_2$	823	CO_2	40	94	Wang et al. (2019b)
$Ce_{1-x}Zr_xO_2$	823	CO_2	15	95	Wang et al. (2019a)
V-Ce-Zr-Al	823	CO_2	62	92	Wang et al. (2019c)
α-Fe_2O_3	823	CO_2	3	95	Wang et al. (2017c)
MnO_x	823	CO_2	35	76	Ren et al. (2017)
Ce-Fe/NSA	823	CO_2	56	95	Present study

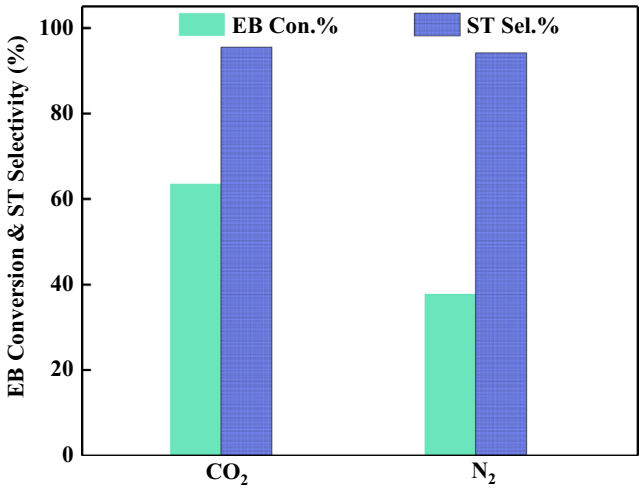

Fig. 7 Catalytic performance of Ce50Fe50/NSA with different feed gases.

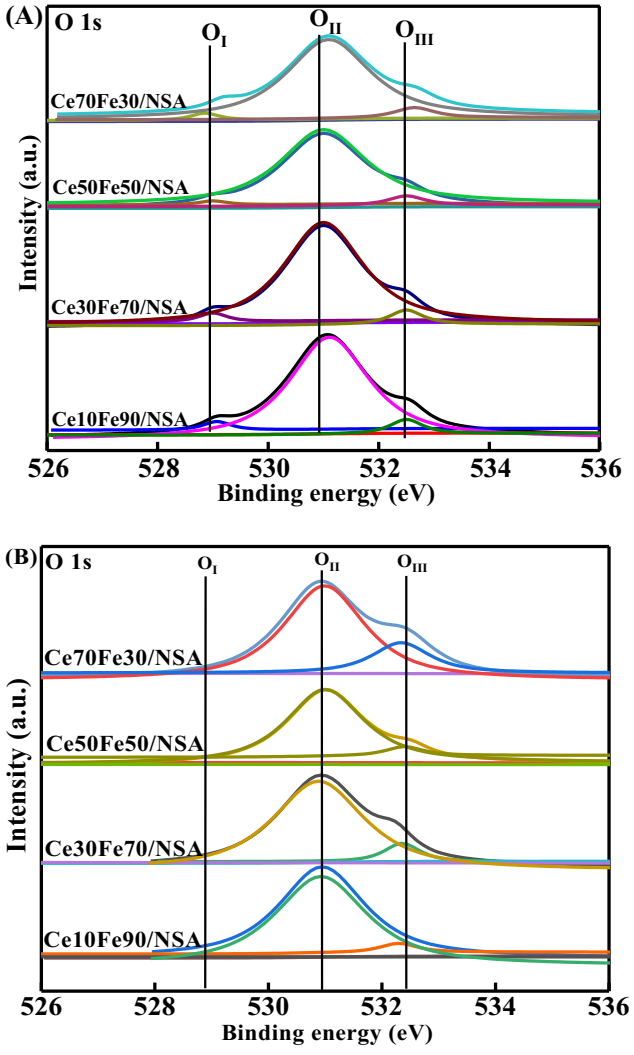

Fig. 8 O 1s XPS spectra of fresh (A) and spent (B) supported CeO_2-Fe_2O_3 binary oxides.

surface-absorbed oxygen (Li et al., 2014). Moreover, the available amount and reversibility of the mobile oxygen species are curial in determining the stability for CO_2-ODEB. Thus, the oxygen species were then investigated. As shown in Fig. 8(A), the O 1s spectrum displayed 3 peaks after deconvolution. The lower binding energy at about 529 eV represents the surface lattice oxygen derived from binary oxides, labeled as O_I, and the broad peak at about 531 eV, marked as O_{II}, may be ascribed to monatomic oxygen (or surface-absorbed oxygen), such as O^{2-}, O_2^{2-} or O^-, which considered as derived from surface oxygen vacancies/defects with unsaturated chemical bonds, can enhance the mobility of the lattice oxygen. The last peak at 532 eV was assigned to the absorbed oxygen, denoted as O_{III}, which could represent the hydroxyl-like groups or other weakly absorbed oxygen species (WEI et al., 2010). The calculated content of each oxygen species was listed in Table 5. The relationship between lattice oxygen (O_I) and monatomic oxygen (O_{II}) and EB conversion before and after the reaction was depicted in Fig. 9. From the results, samples Ce30Fe70/NSA and Ce50Fe50/NSA with a high proportion of O_I and O_{II}, were expected to exhibit higher catalytic activity in the CO_2-ODEB reaction, as confirmed by the value of $(O_I + O_{II})/ O_{III}$ was higher than other samples, the remaining samples generally match well with the trend of EB conversion. Moreover, the changing pattern for the content of $(O_I + O_{II})/ O_{III}$ also matched very well with that for the value of $Ce^{3+}/(Ce^{3+} + Ce^{4+})$ in Table 3, indicating that the con-

Table 5 O 1s XPS data of fresh and spent supported CeO_2-Fe_2O_3 binary oxides.

Sample	Relative content (%)			
	O_I	O_{II}	O_{III}	$(O_I + O_{II})/O_{III}$
(a) Ce10Fe90/NSA	15.0	62.5	22.5	3.52
(b) Ce30Fe70/NSA	14.4	73.7	11.9	7.40
(c) Ce50Fe50/NSA	10.2	81.3	8.5	10.76
(d) Ce70Fe30/NSA	6.3	68.5	25.2	2.96
(a′) Ce10Fe90/NSA-spent	–	60.7	39.3	1.54
(b′) Ce30Fe70/NSA-spent	–	66.1	33.9	1.94
(c′) Ce50Fe50/NSA-spent	–	63.2	36.8	1.72
(d′) Ce70Fe30/NSA-spent	–	58.3	41.7	1.40

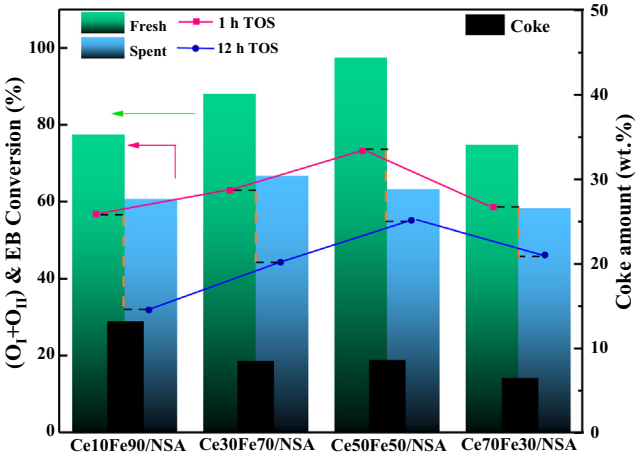

Fig. 9 Mobile oxygen and catalytic performance of supported CeO_2-Fe_2O_3 binary oxides.

tent of O_I + O_{II} is equivalent to the proportion of Ce^{3+}. On the other hand, the higher activity also can be ascribed to the well dispersed CeO_2-Fe_2O_3 binary oxides in hierarchically structured support. As discussed, CeO_2-Fe_2O_3 binary oxides could be located inside the slit-shaped pores, promoting the formation of two types of solid solutions, leading to a higher concentration of surface lattice oxygen (O_I) and monatomic oxygen (O_{II}) (Zhang and Lin, 2011).

Moreover, oxygen species of spent catalysts were also investigated and shown in Fig. 8(B). It can be seen that O_I was almost exhausted during the reaction, as the peaks nearly vanished, and O_{II} also slightly decreased. The comparison of O_I and O_{II} before and after reaction confirmed that the lattice oxygen (O_I) and monatomic oxygen (O_{II}) contributed to higher activity and both played an essential role in the reaction as discussed above. However, the amount of O_{III} was increased, and the $(O_I + O_{II})/ O_{III}$ value of spent catalysts kept the same order as before the reaction, but the gap between each other narrowed, combined the only slightly consumed O_{II} which should have decreased more, and the presence of CO_2 in the reaction, one deduction can be made that, the intertransmission of oxygen species allowed the original O_{III} to replenish O_{II}, and CO_2 served as an oxidant can recover the O_{III}, however, O_I cannot be restored completely.

Furthermore, as indicated by the reaction results, the redox cycle cannot be fully maintained throughout the reaction because of the coke. The deposited coke inhibited the reversibility of the mobile oxygen, leading to the increasing extent of deactivation. It is commonly known that the coke deposition is inevitable under typical conditions for CO_2-ODEB, however, the participation of CO_2 in the reaction may achieve dynamic equilibrium of coke forming and burning (Wang et al., 2010; Liu et al., 2011). The relative deactivation rate (R), defined as $100 \times (X_1 - X_{12})/X_1$, where X was the EB conversion, was then calculated. The deactivation rate of Ce70Fe30/NSA and Ce50Fe50/NSA were 21% and 27%, much lower than Ce10Fe90/NSA and Ce30Fe70/NSA, 42% and 30%, respectively, and pure Fe_2O_3 loaded sample suffered deactivation greatly. The deactivation rate indicated different coke resistance among samples. To get a deep understanding of the generated coke. Acquired spent supported CeO_2-Fe_2O_3 binary oxides were evaluated by TG, as shown in Fig. 10. Clear weight loss can be observed in all samples, and the weight loss can be reasonably attributed to the gasification of the coke. The amount of coke in each sample was different, spent pure Fe_2O_3 loaded sample contained about 14 wt % coke, while spent CeO_2-Fe_2O_3 binary oxides showed less. On the other hand, the gasification temperature varied. Form DTG data, it was obvious that the spent CeO_2-Fe_2O_3 binary oxides exhibited a lower gasification temperature than the pure

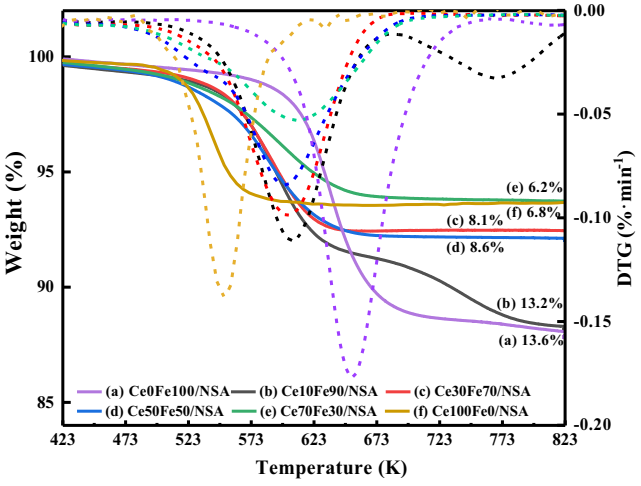

Fig. 10 TG-DTG profiles of spent supported CeO_2-Fe_2O_3 binary oxides.

Fe_2O_3 loaded sample. In Fig. 10, the weight of spent CeO_2-Fe_2O_3 binary oxides begin to drop at about 523 K, while the coke in Ce0Fe100/NSA began to gasification about 100 K higher. The varied coke amount and coke gasification temperatures indicate that the existence of proper amount CeO_2 enhances the coke resistance and coke in CeO_2-Fe_2O_3 binary oxides was easier to be eliminated than pure Fe_2O_3 loaded sample, which may due to the surface of the oxygen species, the relationship between deactivation rate and coke was depicted in Fig. 9.

3.7. Mechanism and simulation

A proposed reaction pathway was shown in Fig. 11. Firstly, ethylbenzene absorbed on the catalyst surface, dehydrogenated to styrene and H-H, mobile oxygen then reacted with H-H produced H_2O (step 1 and 2). The high valence redox couple Fe^{3+}/Ce^{4+} was reduced to Fe^{2+}/Ce^{4+}, as well as the oxygen vacancy was produced, because of the high energy barrier of CO_2 decomposition and kinetically unfavored formation of CO on defective Fe surface, in this case, CeO_2 then donated an oxygen atom to recover the oxygen vacancy, leading to Fe^{3+}/Ce^{3+} (step 3) (He et al., 2011). Then, CO_2 was absorbed and consequently replenished the oxygen vacancy on the CeO_2 surface (step 4). Finally, the oxygen species spread and partially restored the redox couple to Fe^{3+}/Ce^{4+}. In the whole process, the presence of oxygen vacancies and the transmission of the oxygen species could accelerate the adsorption of CO_2 and the diffusion speed of oxygen, thus prompting the entire reaction.

Density functional theory (DFT) calculations were performed to confirm the feasibility under typical conditions, and further understand the reaction pathway proposed in Fig. 11. All computational details and results were presented in Fig. 12. For step 1, ethylbenzene absorbed on the O-terminated Fe_2O_3 surface, then dehydrogenated to produce styrene and H—H, owing to the strong H—O binding, molecular H_2 formation was difficult to form (He et al., 2011). The

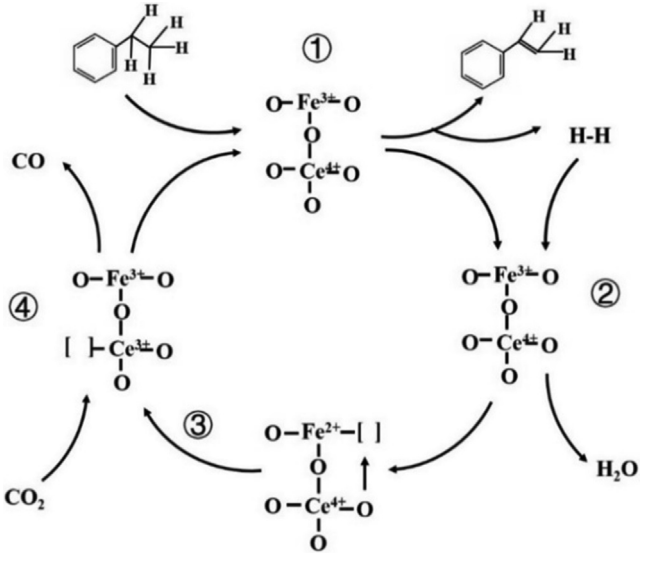

Fig. 11 Proposed reaction scheme of CO_2-ODEB.

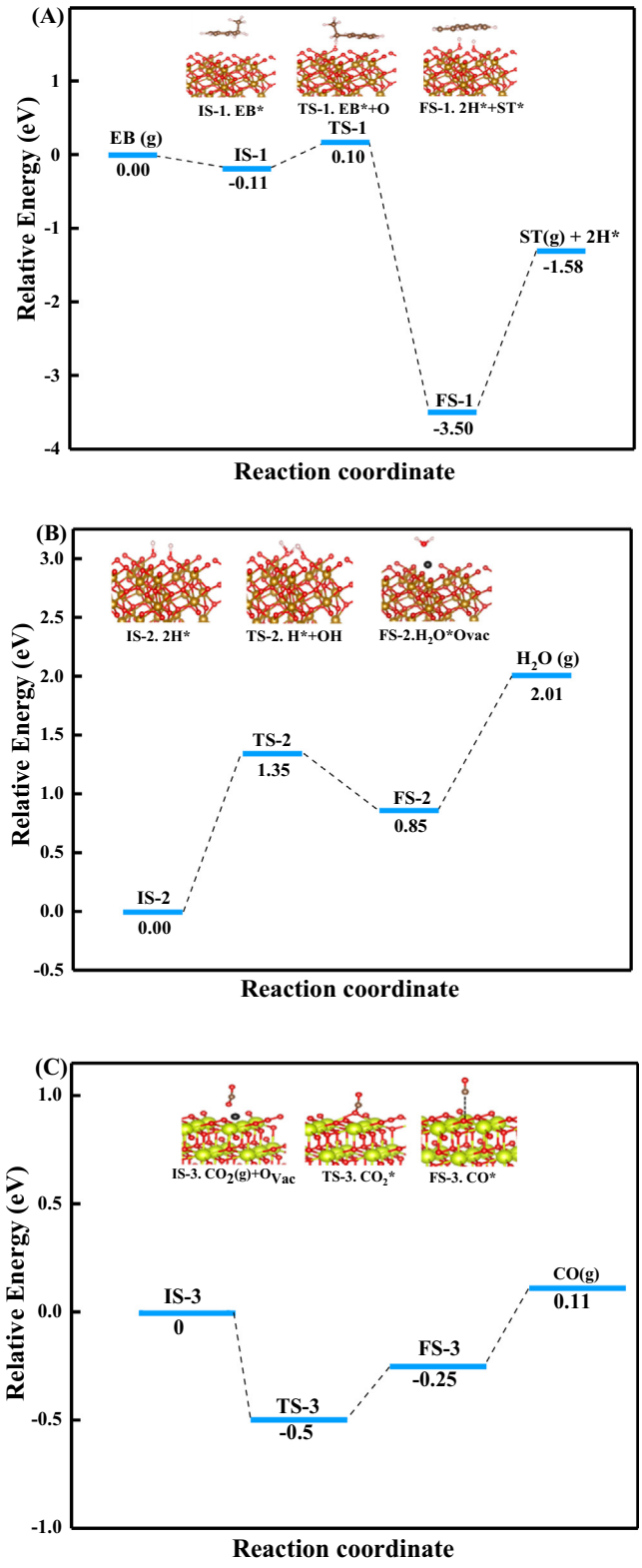

Fig. 12 Potential energy diagrams and transition states of CO_2-ODEB from DFT calculations. (A) Step ①, (B) Step ② and (C) step ④. (IS: Initial states; TS: transition state; FS: final state).

dehydrogenation reaction followed the Mars van Krevelen mechanism, the energy barrier was calculated to be 0.1 eV, and the whole process was exothermic. The following step

2, the dehydrogenated H atoms absorbed at the O site and reacted with an adjacent hydroxyl group to produce H_2O, this elementary reaction was endothermic, and the energy barrier was 1.35 eV. Then the H_2O was desorbed with an energy barrier of 1.16 eV, and the surface of the oxides was reduced. This step is the rate determining step due to the highest energy barrier. The step 4, oxygen vacancy replenishment process, a CO_2 molecule contacted with an oxygen vacancy and provided an O atom to restore the defect and detached as a CO molecule.

4. Conclusions

In summary, the hierarchical structure will be maintained after load CeO_2-Fe_2O_3 binary oxides onto nano-sheet γ-Al_2O_3. The insertion of Ce or Fe species will cause the ion substitution and then form the solid solution. In the case of the catalytic activity, CeO_2-Fe_2O_3 binary oxides show better ethylbenzene conversion and coke resistance than pure Fe_2O_3 loaded sample. Base on the redox mechanism of CO_2-ODEB and characterization results of fresh and spent catalysts, surface lattice oxygen (O_I) and monatomic oxygen (O_{II}) were found to be the key factors in determining the activity for the title reaction. Moreover, the inter-transmission of oxygen species and the presence of CO_2 can refill the oxygen vacancies and restore the redox cycle of CeO_2-Fe_2O_3 binary oxides. The DFT studies verified the reaction pathway, and the oxygen species react with hydrogen act as the rate-determining step, and the oxygen vacancy replenishment process is favorable in studied conditions. With these understandings, the optimization of the synthetic parameters may develop not only a highly active but also a stable catalyst for the title reaction, which is worthy of being done.

Declaration of Competing Interest

The authors declare that they have no known competing financial interests or personal relationships that could have appeared to influence the work reported in this paper.

Acknowledgments

We thank the writing assistance from Emily Schulman, University of Maryland, College Park.

References

Abdollahifar, M., Zamani, R., Beiygie, E., Nekouei, H., 2014. Synthesis of micro-mesopores flowerlike γ-Al2O3 nano-architectures. J. Serbian Chem. Soc. 79, 1007–1017. https://doi.org/10.2298/JSC130903007A.

Ahn, K., Yoo, D.S., Prasad, D.H., Lee, H.-W., Chung, Y.-C., Lee, J.-H., 2012. Role of multivalent Pr in the formation and migration of oxygen vacancy in Pr-doped ceria: experimental and first-principles investigations. Chem. Mater. 24, 4261–4267. https://doi.org/10.1021/cm3022424.

Ansari, M.B., Park, S.-E., 2012. Carbon dioxide utilization as a soft oxidant and promoter in catalysis. Energy Environ. Sci. 5, 9419–9437. https://doi.org/10.1039/C2EE22409G.

Baghalha, M., Ebrahimpour, O., 2007. Structural changes and surface activities of ethylbenzene dehydrogenation catalysts during deactivation. Appl. Catal. A Gen. 326, 143–151. https://doi.org/10.1016/j.apcata.2007.04.008.

Bêche, E., Charvin, P., Perarnau, D., Abanades, S., Flamant, G., 2008. Ce 3d XPS investigation of cerium oxides and mixed cerium oxide (CexTiyOz). Surf. Interface Anal. 40, 264–267. https://doi.org/10.1002/sia.2686.

Blöchl, P.E., 1994. Projector augmented-wave method. Phys. Rev. B 50, 17953–17979. https://doi.org/10.1103/PhysRevB.50.17953.

Brünig, J., Csendes, Z., Weber, S., Gorgas, N., Bittner, R.W., Limbeck, A., Bica, K., Hoffmann, H., Kirchner, K., 2018. Chemoselective supported ionic-liquid-phase (SILP) aldehyde hydrogenation catalyzed by an Fe(II) PNP pincer complex. ACS Catal. 8, 1048–1051. https://doi.org/10.1021/acscatal.7b04149.

Coulter, K., Goodman, D.W., Moore, R.G., 1995. Kinetics of the dehydrogenation of ethylbenzene to styrene over unpromoted and K-promoted model iron oxide catalysts. Catal. Lett. 31, 1–8. https://doi.org/10.1007/BF00817027.

Diao, J., Feng, Z., Huang, R., Liu, H., Hamid, S.B.A., Su, D.S., 2016. Selective and stable ethylbenzene dehydrogenation to styrene over nanodiamonds under oxygen-lean conditions. ChemSusChem 9, 662–666. https://doi.org/10.1002/cssc.201501516.

Diao, J., Zhang, Y., Zhang, J., Wang, J., Liu, H., Su, D.S., 2017. Fabrication of MgO–rGO hybrid catalysts with a sandwich structure for enhanced ethylbenzene dehydrogenation performance. Chem. Commun. 53, 11322–11325. https://doi.org/10.1039/C7CC05283A.

Ebiad, M.A., Abd El-Hafiz, D.R., Elsalamony, R.A., Mohamed, L.S., 2012. Ni supported high surface area CeO2–ZrO2 catalysts for hydrogen production from ethanol steam reforming. RSC Adv. 2, 8145–8156. https://doi.org/10.1039/C2RA20258A.

Fan, H.-X., Feng, J., Li, W.-Y., 2019. Promotional effect of oxygen storage capacity on oxy-dehydrogenation of ethylbenzene with CO2 over κ-Ce2Zr2O8(111). Appl. Surf. Sci. 486, 411–419. https://doi.org/10.1016/j.apsusc.2019.04.244.

Figueiredo, W.T., Della Mea, G.B., Segala, M., Baptista, D.L., Escudero, C., Pérez-Dieste, V., Bernardi, F., 2019. Understanding the strong metal-support interaction (SMSI) effect in CuxNi1–x/CeO2 ($0 < x < 1$) nanoparticles for enhanced catalysis. ACS Appl. Nano Mater. 2, 2559–2573. https://doi.org/10.1021/acsanm.9b00569.

Guo, M., Lu, J., Wu, Y., Wang, Y., Luo, M., 2011. UV and visible Raman studies of oxygen vacancies in rare-earth-doped ceria. Langmuir 27, 3872–3877. https://doi.org/10.1021/la200292f.

He, X.-X., Fan, C., Gu, X.-Y., Chen, D., Zhu, Y.-A., 2011. Role of CO2 in ethylbenzene dehydrogenation over Fe2O3(0 0 0 1) from first principles. J. Mol. Catal. A Chem. 344, 53–61. https://doi.org/10.1016/j.molcata.2011.05.002.

Hedayati, A., Azad, A.-M., Rydén, M., Leion, H., Mattisson, T., 2012. Evaluation of novel ceria-supported metal oxides as oxygen carriers for chemical-looping combustion. Ind. Eng. Chem. Res. 51, 12796–12806. https://doi.org/10.1021/ie300168j.

Hong, W.-J., Iwamoto, S., Inoue, M., 2010. Direct decomposition of NO on Ba catalysts supported on Ce–Fe mixed oxides. Catal. Lett. 135, 190–196. https://doi.org/10.1007/s10562-010-0296-1.

Kano, Y., Ohshima, M., Kurokawa, H., Miura, H., 2013. Dehydrogenation of ethylbenzene over Fe–Ce–Rb and Fe–Ce–Cs mixed oxide catalysts. React. Kinet. Mech. Catal. 109, 29–41. https://doi.org/10.1007/s11144-013-0549-2.

Kresse, G., Furthmüller, J., 1996. Efficiency of ab-initio total energy calculations for metals and semiconductors using a plane-wave basis set. Comput. Mater. Sci. 6, 15–50. https://doi.org/10.1016/0927-0256(96)00008-0.

Kresse, G., Hafner, J., 1993. Ab initio molecular dynamics for open-shell transition metals. Phys. Rev. B 48, 13115–13118. https://doi.org/10.1103/PhysRevB.48.13115.

Kuntaiah, K., Sudarsanam, P., Reddy, B.M., Vinu, A., 2013. Nanocrystalline Ce1−xSmxO2−δ (x = 0.4) solid solutions: struc-

tural characterization versus CO oxidation. RSC Adv. 3, 7953–7962. https://doi.org/10.1039/C3RA23491F.

Kurnatowska, M., Mista, W., Mazur, P., Kepinski, L., 2014. Nanocrystalline Ce1−xRuxO2 – Microstructure, stability and activity in CO and soot oxidation. Appl. Catal. B Environ. 148–149, 123–135. https://doi.org/10.1016/j.apcatb.2013.10.047.

Kuśtrowski, P., Segura, Y., Chmielarz, L., Surman, J., Dziembaj, R., Cool, P., Vansant, E.F., 2006. VOx supported SBA-15 catalysts for the oxidative dehydrogenation of ethylbenzene to styrene in the presence of N2O. Catal. Today 114, 307–313. https://doi.org/10.1016/j.cattod.2006.02.014.

Laguna, O.H., Centeno, M.A., Boutonnet, M., Odriozola, J.A., 2011. Fe-doped ceria solids synthesized by the microemulsion method for CO oxidation reactions. Appl. Catal. B Environ. 106, 621–629. https://doi.org/10.1016/j.apcatb.2011.06.025.

Lee, E.H., 1974. Iron Oxide catalysts for dehydrogenation of ethylbenzene in the presence of steam. Catal. Rev. 8, 285–305. https://doi.org/10.1080/01614947408071864.

Li, G., Smith, R.L., Inomata, H., 2001. Synthesis of nanoscale Ce1-xFexO2 solid solutions via a low-temperature approach. J. Am. Chem. Soc. 123, 11091–11092. https://doi.org/10.1021/ja016502+.

Li, K., Haneda, M., Ning, P., Wang, H., Ozawa, M., 2014. Microstructure and oxygen evolution of Fe–Ce mixed oxides by redox treatment. Appl. Surf. Sci. 289, 378–383. https://doi.org/10.1016/j.apsusc.2013.10.170.

Liang, C., Ma, Z., Lin, H., Ding, L., Qiu, J., Frandsen, W., Su, D., 2009. Template preparation of nanoscale CexFe1−xO2 solid solutions and their catalytic properties for ethanol steam reforming. J. Mater. Chem. 19, 1417–1424. https://doi.org/10.1039/B817942E.

Liu, H., Diao, J., Wang, Q., Gu, S., Chen, T., Miao, C., Yang, W., Su, D., 2014. A nanodiamond/CNT–SiC monolith as a novel metal free catalyst for ethylbenzene direct dehydrogenation to styrene. Chem. Commun. 50, 7810–7812. https://doi.org/10.1039/C4CC01693A.

Liu, Z.-W., Wang, C., Fan, W.-B., Liu, Z.-T., Hao, Q.-Q., Long, X., Lu, J., Wang, J.-G., Qin, Z.-F., Su, D.S., 2011. V2O5/Ce0.6Zr0.4O2-Al2O3 as an efficient catalyst for the oxidative dehydrogenation of ethylbenzene with carbon dioxide. ChemSusChem 4, 341–345. https://doi.org/10.1002/cssc.201000351.

Mimura, N., Saito, M., 2000. Dehydrogenation of ethylbenzene to styrene over Fe2O3/Al2O3 catalysts in the presence of carbon dioxide. Catal. Today 55, 173–178. https://doi.org/10.1016/S0920-5861(99)00236-9.

Mimura, N., Takahara, I., Saito, M., Hattori, T., Ohkuma, K., Ando, M., 1998. Dehydrogenation of ethylbenzene over iron oxide-based catalyst in the presence of carbon dioxide. In: Inui, T., Anpo, M., Izui, K., Yanagida, S. (Eds.), Advances in Chemical Conversions for Mitigating Carbon Dioxide. Elsevier, pp. 415–418.

Oh, S.C., Nguyendo, T., He, Y., Filie, A., Wu, Y., Tran, D.T., Lee, I. C., Liu, D., 2017. External surface and pore mouth catalysis in hydrolysis of inulin over zeolites with different micropore topologies and mesoporosities. Catal. Sci. Technol. 7, 1153–1166. https://doi.org/10.1039/C6CY02613C.

Patterson, A.L., 1939. The Scherrer formula for X-ray particle size determination. Phys. Rev. 56, 978–982. https://doi.org/10.1103/PhysRev.56.978.

Perdew, J.P., Burke, K., Ernzerhof, M., 1996. Generalized gradient approximation made simple. Phys. Rev. Lett. 77, 3865–3868. https://doi.org/10.1103/PhysRevLett.77.3865.

Pérez-Alonso, F.J., López Granados, M., Ojeda, M., Terreros, P., Rojas, S., Herranz, T., Fierro, J.L.G., Gracia, M., Gancedo, J.R., 2005. Chemical structures of coprecipitated Fe−Ce mixed oxides. Chem. Mater. 17, 2329–2339. https://doi.org/10.1021/cm0477669.

Pérez-Alonso, F.J., Melián-Cabrera, I., Granados, M., Kapteijn, F., Fierro, J.L.G., 2006. Synergy of FexCe1−xO2 mixed oxides for N2O decomposition. J. Catal. 239, 340–346. https://doi.org/10.1016/j.jcat.2006.02.008.

Qiao, D., Lu, G., Liu, X., Guo, Y., Wang, Y., Guo, Y., 2011. Preparation of Ce1−xFexO2 solid solution and its catalytic performance for oxidation of CH4 and CO. J. Mater. Sci. 46, 3500–3506. https://doi.org/10.1007/s10853-011-5256-7.

Ren, K., Song, J., Song, Y.-H., Wang, H., Liu, Z., Liu, Z.-T., Jiang, J., Liu, Z.-W., 2017. Catalytic behavior of manganese oxides for oxidative dehydrogenation of ethylbenzene with carbon dioxide. J. CO2 Util. 22, 63–70.

Sheppard, D., Terrell, R., Henkelman, G., 2008. Optimization methods for finding minimum energy paths. J. Chem. Phys. 128, 134106. https://doi.org/10.1063/1.2841941.

Su, Y.-Q., Liu, J.-X., Filot, I.A.W., Zhang, L., Hensen, E.J.M., 2018. Highly active and stable CH4 oxidation by substitution of Ce4+ by two Pd2+ ions in CeO2(111). ACS Catal. 8, 6552–6559. https://doi.org/10.1021/acscatal.8b01477.

Sun, A., Qin, Z., Chen, S., Wang, J., 2004. Role of carbon dioxide in the ethylbenzene dehydrogenation coupled with reverse water–gas shift. J. Mol. Catal. A Chem. 210, 189–195. https://doi.org/10.1016/j.molcata.2003.09.016.

Wang, C., Fan, W.-B., Liu, Z.-T., Lu, J., Liu, Z.-W., Qin, Z.-F., Wang, J.-G., 2010. The dehydrogenation of ethylbenzene with CO2 over V2O5/CexZr1−xO2 prepared with different methods. J. Mol. Catal. A Chem. 329, 64–70. https://doi.org/10.1016/j.molcata.2010.06.019.

Wang, C., Shi, J., Cui, X., Zhang, J., Zhang, C., Wang, L., Lv, B., 2017c. The role of CO2 in dehydrogenation of ethylbenzene over pure α-Fe2O3 catalysts with different facets. J. Catal. 345, 104–112. https://doi.org/10.1016/j.jcat.2016.10.032.

Wang, H., Cao, F.-X., Song, Y.-H., Yang, G.-Q., Ge, H.-Q., Liu, Z.-T., Qu, Y.-Q., Liu, Z.-W., 2019a. Two-step hydrothermally synthesized Ce1-xZrxO2 for oxidative dehydrogenation of ethylbenzene with carbon dioxide. J. CO2 Util. 34, 99–107.

Wang, H., Yang, G.-Q., Song, Y.-H., Liu, Z.-T., Liu, Z.-W., 2019b. Defect-rich Ce1-xZrxO2 solid solutions for oxidative dehydrogenation of ethylbenzene with CO2. Catal. Today 324, 39–48. https://doi.org/10.1016/j.cattod.2018.07.051.

Wang, H., Zhu, W., Yang, G.-Q., Zhang, Y.-W., Song, Y.-H., Jiang, N., Liu, Z.-T., Liu, Z.-W., 2019c. Insights into the oxidative dehydrogenation of ethylbenzene with CO2 catalyzed by the ordered mesoporous V2O5–Ce0.5Zr0.5O2–Al2O3. Ind. Eng. Chem. Res. 58, 21372–21381. https://doi.org/10.1021/acs.iecr.9b04286.

Wang, Q., Li, X., Li, W., Feng, J., 2014. Promoting effect of Fe in oxidative dehydrogenation of ethylbenzene to styrene with CO2 (I) preparation and performance of Ce1−xFexO2 catalyst. Catal. Commun. 50, 21–24. https://doi.org/10.1016/j.catcom.2014.02.014.

Wang, T., Guan, X., Lu, H., Liu, Z., Ji, M., 2017a. Nanoflake-assembled Al2O3 -supported CeO2-ZrO 2 as an efficient catalyst for oxidative dehydrogenation of ethylbenzene with CO2. Appl. Surf. Sci. 398, 1–8. https://doi.org/10.1016/j.apsusc.2016.11.180.

Wang, T., Qi, L., Lu, H., Ji, M., 2017b. Flower-like Al2O3-supported iron oxides as an efficient catalyst for oxidative dehydrogenation of ethlybenzene with CO2. J. CO2 Util. 17, 162–169. https://doi.org/10.1016/j.jcou.2016.12.005.

Wei, Y., Wang, H., Li, K., 2010. Ce-Fe-O mixed oxide as oxygen carrier for the direct partial oxidation of methane to syngas. J. Rare Earths 28, 560–565. https://doi.org/10.1016/S1002-0721(09)60154-X.

Wu, J.-C., Liu, D.-S., Ko, A.-N., 1993. Dehydrogenation of ethylbenzene over TiO2-Fe2O3 and ZrO2-Fe2O3 mixed oxide catalysts. Catal. Letters 20, 191–201. https://doi.org/10.1007/BF00769292.

Yao, X., Tang, C., Ji, Z., Dai, Y., Cao, Y., Gao, F., Dong, L., Chen, Y., 2013. Investigation of the physicochemical properties and catalytic activities of Ce0.67M0.33O2 (M = Zr4+, Ti4+, Sn4+) solid solutions for NO removal by CO. Catal. Sci. Technol. 3, 688–698. https://doi.org/10.1039/C2CY20610B.

Yin, S., Minamidate, Y., Tonouchi, S., Goto, T., Dong, Q., Yamane, H., Sato, T., 2012. Solution synthesis of homogeneous plate-like

multifunctional CeO2 particles. RSC Adv. 2, 5976–5982. https://doi.org/10.1039/C2RA20280H.

Zhang, C., Lin, J., 2011. Visible-light induced oxo-bridged ZrIV−O−CeIII redox centre in tetragonal ZrO2–CeO2 solid solution for degradation of organic pollutants. Phys. Chem. Chem. Phys. 13, 3896–3905. https://doi.org/10.1039/C0CP01782E.

Zhang, Z., Han, D., Wei, S., Zhang, Y., 2010. Determination of active site densities and mechanisms for soot combustion with O2 on Fe-doped CeO2 mixed oxides. J. Catal. 276, 16–23. https://doi.org/10.1016/j.jcat.2010.08.017.

Zhao, T.-J., Sun, W.-Z., Gu, X.-Y., Rønning, M., Chen, D., Dai, Y.-C., Yuan, W.-K., Holmen, A., 2007. Rational design of the carbon nanofiber catalysts for oxidative dehydrogenation of ethylbenzene. Appl. Catal. A Gen. 323, 135–146. https://doi.org/10.1016/j.apcata.2007.02.008.

Zhou, Y., Zhou, J., 2010. Growth and surface structure of Ti-doped CeOx(111) thin films. J. Phys. Chem. Lett. 1, 1714–1720. https://doi.org/10.1021/jz1004297.

Zhu, X., Sun, L., Zheng, Y., Wang, H., Wei, Y., 2014. CeO2 modified Fe2O3 for the chemical hydrogen storage and production via cyclic water splitting. Int. J. Hydrogen Energy 39, 13381–13388. https://doi.org/10.1016/j.ijhydene.2014.04.136.

Zhu, X., Wei, Y., Wang, H., Li, K., 2013. Ce–Fe oxygen carriers for chemical-looping steam methane reforming. Int. J. Hydrogen Energy 38, 4492–4501. https://doi.org/10.1016/j.ijhydene.2013.01.115.

Zuo, Y., Huang, X., Li, L., Li, G., 2013. An ultra-stable nanosized Ce0.9Fe0.1O2 solid solution with an excellent catalytic performance towards CH4 oxidation. J. Mater. Chem. A 1, 374–380. https://doi.org/10.1039/C2TA00167E.